Available online at www.sciencedirect.com

SciVerse ScienceDirect

Ceramics International 39 (2013) 1807–1819

CERAMICS INTERNATIONAL

www.elsevier.com/locate/ceramint

Influence of Cr^{3+} ion on the structural, ac conductivity and magnetic properties of nanocrystalline Ni–Mg ferrite

Mohd. Hashim[a,*], Alimuddin[a], Shalendra Kumar[b], Sagar E. Shirsath[c], R.K. Kotnala[d], Jyoti Shah[d], Ravi Kumar[e]

[a]Deptartment of Applied Physics, Aligarh Muslim University, Aligarh 202002, India
[b]Department of Physics, Pohang University of Science and Technology, Pohang 790–784, Republic of Korea
[c]Spin Device Technology Center, Faculty of Engineering, Shinshu University, Nagano 380-8553, Japan
[d]National Physical Laboratory (CSIR), Dr. K.S. Krishnan Road, New Delhi 110012, India
[e]Centre for Material Science Engineering, National Institute of Technology, Hamirpur, 177005 Himachal Pradesh, India

Received 21 March 2012; received in revised form 10 August 2012; accepted 10 August 2012
Available online 18 August 2012

Abstract

Nanocrystalline samples of the Ni–Mg ferrite with the general chemical formula $Ni_{0.5}Mg_{0.5}Cr_xFe_{2-x}O_4$ ($0 \le x \le 1.0$, in the step of 0.2) have been synthesized by the citrate-gel auto combustion route. The synthesized samples were characterized by means of XRD, EDAX, FT-IR, UV–visible, dielectric, ac impedance spectroscopy, and AFM, SEM, TEM and FC/ZFC measurements. X-ray powder diffraction of all the samples were carried out at room temperature to check the formation of the required products and structural related properties. The elemental analysis as obtained from the EDAX measurement is in close agreement with the expected composition from the stoichiometry of the reactant solutions. IR studies confirm two main absorption bands in the frequency range of 400–800 cm^{-1}, arising due to the tetrahedral (A) and octahedral [B] stretching vibrations. Impedance spectroscopy techniques have been used to study the effect of grain and grain boundary on the electrical properties of the prepared samples. The samples were zero field cooled (ZFC) to 100 K. Typical blocking temperature effects were observed below the temperature of about 129 K. The obtained results have been discussed so as to bring out the role of chromium substitution on the structural, dielectric and magnetic properties of Ni–Mg ferrites.

Keywords: C. Dielectric properties; C. Magnetic properties; Ferrite nanoparticels; FT-IR

1. Introduction

Recently, a variety of new and somewhat exotic technical terms having the prefix "nano"—nano-structured, nano-scale, nano-phase, nano-crystalline, nano-lithography, nano-electronics, etc., had entered the vocabulary of the material scientists and the advanced materials industry. Correspondingly, the last two decades have witnessed a tremendous increase in the interest of the academics and the industry in material science that is described by these new terminology nanostructured materials. The emergence of nanotechnology has made the study of ferrites at nanoscale quite an interesting subject, both from the fundamental and application point of view. This new class of materials shows properties that are vastly superior to those exhibited by the single crystalline, conventional polycrystalline and amorphous materials and is of great theoretical and technological importance. There is a renewed interest to explore what happens when the physical dimension of a bulk magnetic material is reduced to be comparable to or smaller than a magnetically critical size such as the magnetic domain wall width in nanoscopic region. Below a critical size, single domain magnetic particles behave in contrast to the multidomain structure of the bulk magnetic materials. The properties of the nanocrystalline materials are varied from those of corresponding bulk materials, due to their small grain size.

*Corresponding author. Tel.: +91 9359380185.
E-mail address: md.hashim09@gmail.com (Mohd. Hashim).

0272-8842/$ - see front matter © 2012 Elsevier Ltd and Techna Group S.r.l. All rights reserved.
http://dx.doi.org/10.1016/j.ceramint.2012.08.028

In the nanocrystalline materials a large percentage of atoms is available at their grain boundaries and therefore they find more chances of interaction between the grains. Ferrites with AB_2O_4 formula crystallize either in a normal spinel structure or in an inverse spinel structure. In a normal spinel structure, the A^{2+} cations occupy the tetrahedral site, whereas the B^{3+} cations occupy the octahedral site. In an inverse spinel structure, half of the octahedral coordination sites are occupied by A^{2+} cations and the remaining half as well as all the tetrahedral coordination sites are occupied by the B^{3+} cations. In this cubic symmetry the metal ions are distributed over the two lattice sites; namely tetrahedral A-sites and octahedral B-sites. The tetrahedral site is surrounded by four oxygen ions while the octahedral site is surrounded by six oxygen ions as shown in Fig. 1. The crystallographic, electrical and magnetic properties of these ferrites substantially depend on their method of preparation, chemical composition, sintering temperature, doping additives, and particle size etc. [1–3], which controls the microstructure forming of the high resistive boundaries between the constituents grains. Properties of ferrites have also been strongly affected when the particle size approaches a critical diameter, below which each particle is considered as a single domain [4]. Both the $NiFe_2O_4$ and $MgFe_2O_4$ are well-known inverse spinel structures where divalent Mg^{2+} and Ni^{2+} (A^{2+}) ions occupy B-sites and Fe^{3+} (B^{3+}) ions are distributed equally over the A and B-sites [5,6]. Recently, several methods have been employed to synthesize highly crystalline and uniformly sized magnetic nanoparticles of ferrite [7–9]. The citrate-gel auto combustion method has gained scientific and technological importance during the last decades. This process offers many advantages as compared to the conventional powder route, such as low temperature processing and/or better homogeneity for the synthesis of multi-component materials and thus formation of the nano-range particles of powders. Several researchers have studied the effects of Cr^{3+} substitution in the spinel structure of ferrites [10,11]. However, we have not found any reports in the literature on the Cr^{3+} substituted Ni–Mg ferrite powders obtained by the citrate-gel auto combustion method. In this work we have investigated the $Ni_{0.5}Mg_{0.5}Fe_{2-x}Cr_xO_4$ ($0 \le x \le 1.0$) series with a view to determine the effect of substitution of Cr^{3+} on the structural, electrical and magnetic properties of $Ni_{0.5}Mg_{0.5}Fe_{2-x}Cr_xO_4$.

2. Experimental procedure

Ferrites with different compositions of Cr^{3+} ions with the chemical formula $Ni_{0.5}Mg_{0.5}Fe_{2-x}Cr_xO_4$ ($0 \le x \le 1.0$) have been prepared by the citrate-gel auto combustion method using the high purity 'AR' grade of $Ni(NO_3)_2 \cdot 6H_20$, $Mg(NO_3)_2 \cdot 6H_2O$, $Cr(NO_3)_3 \cdot 9H_2O$, and $Fe(NO_3)_3 \cdot 9H_2O$ as starting materials for the synthesis. Metal nitrates have been taken in the required stoichiometric ratio and dissolved in a minimum amount of double distilled water and mixed together. The mixed metal nitrate solution was then added to the citric acid solution in 1:1 molar ratio. Analytical grade liquor ammonia (30%) was then added under constant stirring in order to maintain the pH = 7. The resulting solution was continuously heated on the magnetic stirrer at 70 °C up to dryness. The obtained gel was annealed at 200 °C for 24 h and then ground for half an hour till a fine powder is obtained. The powder formed was heated again for 6 h at

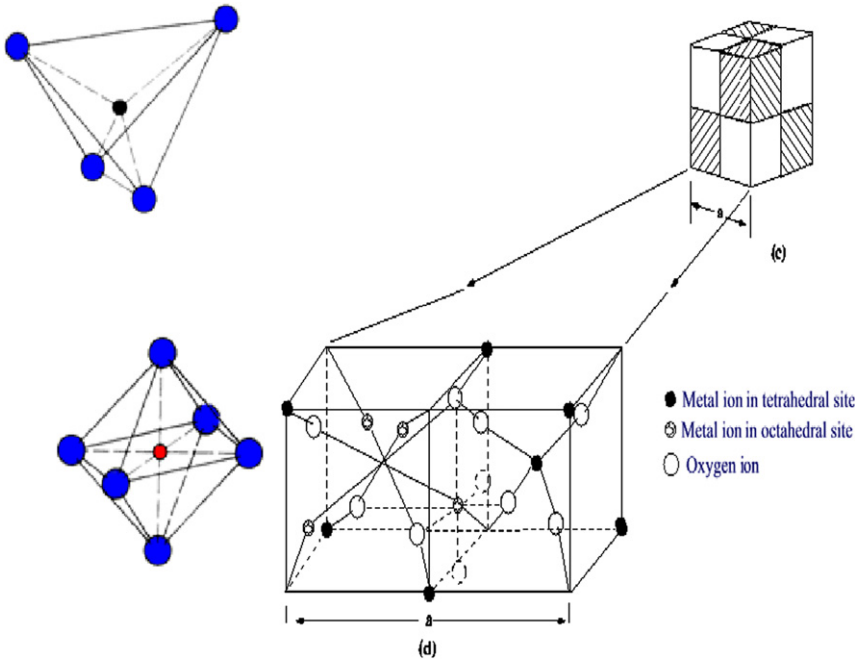

Fig. 1. Schematic of the crystallographic structure of the closed-packed face-centered cubic.

600 °C to remove any organic material present in the system and then finally ground for half an hour [12]. For pellet formation, the powder was mixed with 2% polyvinyl alcohol (binder) and then pressed uniaxially at a pressure of 6 t/cm^2 for 5 min. X-ray powder diffraction (XRD) patterns have been carried out on a Rikagu Miniflex (II) with CuKα radiation at a sweep rate of 2°/min. The morphological studies were done by using AFM (Digital instruments Nanoscope-E, with Si3N4 100 nm cantilever, 0.58 N/m force constant) measurements in contact mode. Field emission scanning electron microscopy (FE-SEM) images were obtained using a TESCAN, MIRA II LMH microscope. The composition was determined by energy dispersive X-ray spectroscopy (EDAX, Inca Oxford,

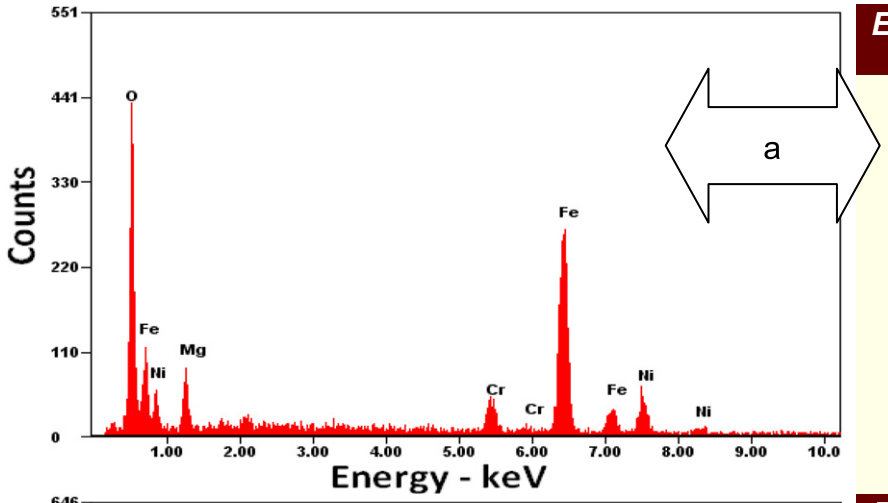

Element	Wt%	At%
OK	24.95	51.09
MgK	06.63	08.94
CrK	04.95	03.12
FeK	49.72	29.17
NiK	13.75	07.67

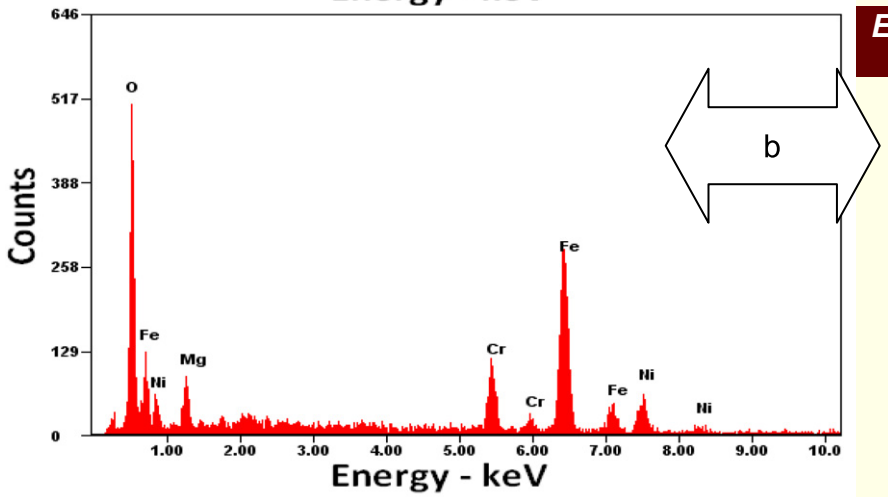

Element	Wt%	At%
OK	25.25	51.36
MgK	06.66	08.92
CrK	09.90	06.20
FeK	44.73	26.06
NiK	13.46	07.46

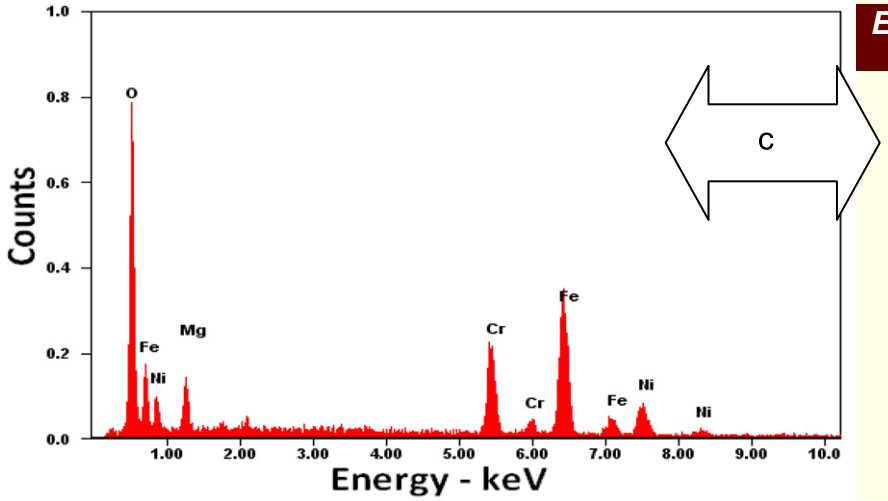

Element	Wt%	At%
OK	28.06	54.65
MgK	06.80	08.72
CrK	14.84	08.90
FeK	37.98	21.20
NiK	12.32	06.54

Fig. 2. EDAX of (a) x=0.2, (b) x=0.4 and (c) x=0.8.

attached to the FE-SEM). TEM measurements were performed using FEI-Tecnai-20 transmission electron microscope. Fourier transform infrared (FT-IR) spectroscopic analysis using KBr pellets was performed using a Jasco model FT-IR 310 spectrophotometer. The capacitance, dielectric and impedance spectroscopy measurements were carried out in the frequency range 42 Hz–5 MHz using LCR HI-Tester (HIOKI 3532-50). The dielectric measurements were carried out in a sintered pellet form; pellets are also sintered for 4 h at 600 °C prior to dielectric measurements. The surfaces of all the samples were polished well to be parallel and smooth, and then coated with the silver paste as contact material for the dielectric measurements. Optical absorption spectra were recorded with the conventional two beam method using a Hitachi UV-3300, UV–visible spectrometer. The magnetization of the samples was also field cooled (FC) and zero field cooled (ZFC) with an external applied magnetic field of 100 Oe. The ZFC–FC measurements were carried out in the temperature range of 80–300 K.

3. Results and discussion

3.1. Structural properties

EDAX analysis were done to determine the chemical composition of the sample to support our observations on the structure of the Ni–Mg ferrite. Results of EDAX analysis of the typical samples are given in Fig. 2a–c. It is observed from the figure that, the Fe^{3+} ions have high concentration as would be expected at low concentration of Cr^{3+} ions. As the Cr^{3+} content goes on increasing, the percentage of Fe^{3+} ions decreased. The atomic weight percentages of the various cations in the $Ni_{0.5}Mg_{0.5}Fe_{1.8}Cr_{0.2}O_4$ (Fig. 2a) samples are found to be O^{2-} (51.09), Mg^{2+} (8.94), Ni^{2+} (7.67), Cr^{3+} (3.12) and Fe (29.17). In the case of the highest Cr^{3+} ion doped sample $Ni_{0.5}Mg_{0.5}Fe_{1.2}Cr_{0.8}O_4$ (Fig. 2c) atomic weight percentages are found to be O^{2-} (54.65), Mg^{2+} (8.72), Cr^{3+} (8.90), Ni^{2+} (6.54) and Fe (21.20). The elemental analysis as obtained from EDAX is in close agreement with the starting composition used for the synthesis. The EDAX quantification can be influenced by the surface crystalline defects of the nanoparticles. This can also be taken into account to explain the difference between the values of the atomic ratio as determined by EDAX and the expected value.

XRD studies of the samples have proved the formation of the single phase cubic spinel structure for all the samples and no detrimental intermediate phase is observed. Fig. 3 displays the structural characterization for all the samples carried out by X-ray diffraction equipped with CuKα radiation (λ=1.5406 Å). The hkl and d-values obtained from the XRD data are listed in Table 1. The lattice constant (a) values have been computed by using the d-spacing values and the respective (h, k, l) parameters from

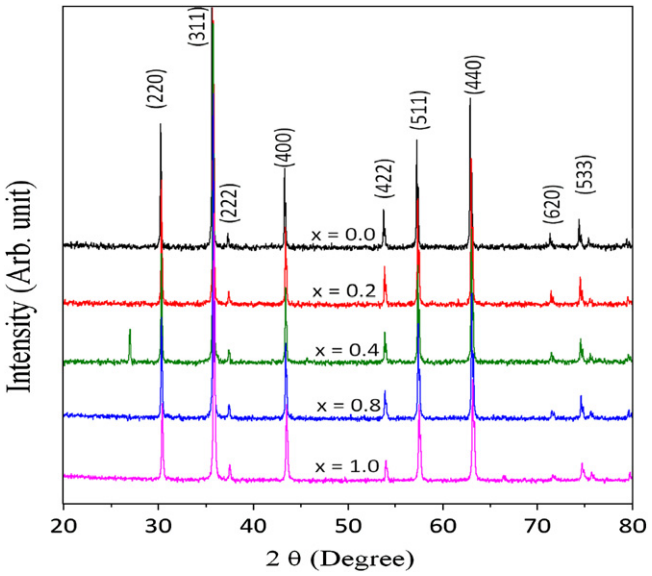

Fig. 3. X-ray diffraction patterns of $Ni_{0.5}Mg_{0.5}Fe_{2-x}Cr_xO_4$ (for x=0.0, 0.2, 0.4 and 0.6).

the classical formula as given below.

$$a = \frac{\lambda}{2}\frac{\sqrt{[h^2+k^2+l^2]}}{\sin\theta} \quad (1)$$

The variation of lattice constant as a function of chromium concentration is shown in Fig. 4 for various $Ni_{0.5}Mg_{0.5}Fe_{2-x}Cr_xO_4$ ferrites. It can be seen that the lattice constant decreased proportionally to the doping contents. The decrease in lattice constant value can be explained on the basis of Vegard's law [13]. According to this law, the linear variation in the lattice constant is due to the ionic radii of the doped and the replacing ion. In the present case we are replacing Fe^{3+} ion with Cr^{3+} ion, as the ionic radius of Cr^{3+} ion is smaller, (0.064 nm) compared to the radius of Fe^{3+} ion (0.067 nm). Thus the substitution of Fe^{3+} ion with Cr^{3+} results in a decrease in lattice constant of this ferrite material. The average crystallite size of the nanophase synthesized particles was determined by using the following Debye–Scherer formula [14] and found in the range of 35–31 nm as shown in Fig. 4:

$$t_{hkl} = \frac{0.98\lambda}{\beta_{hkl}\cos\theta_{hkl}} \quad (2)$$

where λ is the X-ray wavelength of the CuKα radiation (λ=1.5406 Å), θ_{hkl} is the Bragg diffraction angle and β_{hkl} is the full width at half maximum (FWHM) in radians of the main peak in the X-ray diffraction pattern calculated by using Gaussian fitting. The values of the crystallite size are demonstrated in Fig. 4, and it decreases from 35 to 31 nm with increase in Cr content x.

Fig. 5 shows the AFM micrographs, where we have observed that the grains are of different shapes and sizes. FE-SEM micrographs of all the powder samples are shown in Fig. 6. The observed grains were cubic-shaped platelets. The average grain size obviously tends to decrease with

Table 1
Lattice constants (a), Miller indices hkl and interplaner spacing (d) for $Ni_{0.5}Mg_{0.5}Fe_{2-x}Cr_xO_4$ ferrite.

h,k,l	0.0 a=8.450 (Å)	0.2 a=8.436 (Å)	0.4 a=8.431 (Å)	0.6 a=8.428 (Å)	0.8 a=8.425 (Å)	1.0 a=8.423 (Å)
220	2.987	2.983	2.981	2.980	2.979	2.978
311	2.548	2.544	2.542	2.541	2.540	2.540
400	2.112	2.109	2.107	2.107	2.106	2.105
422	1.725	1.722	1.721	1.720	1.720	1.719
333	1.626	1.623	1.622	1.622	1.621	1.621
440	1.493	1.491	1.490	1.490	1.489	1.489

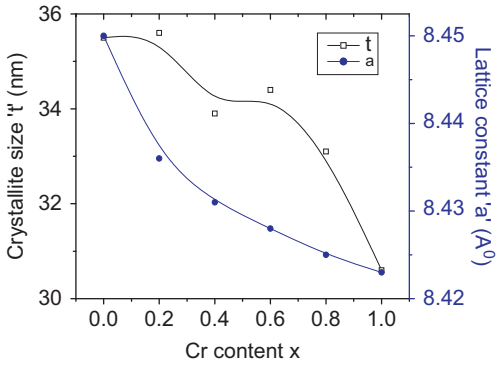

Fig. 4. Variation of lattice constant (a) and crystallite size (t) with Cr content x.

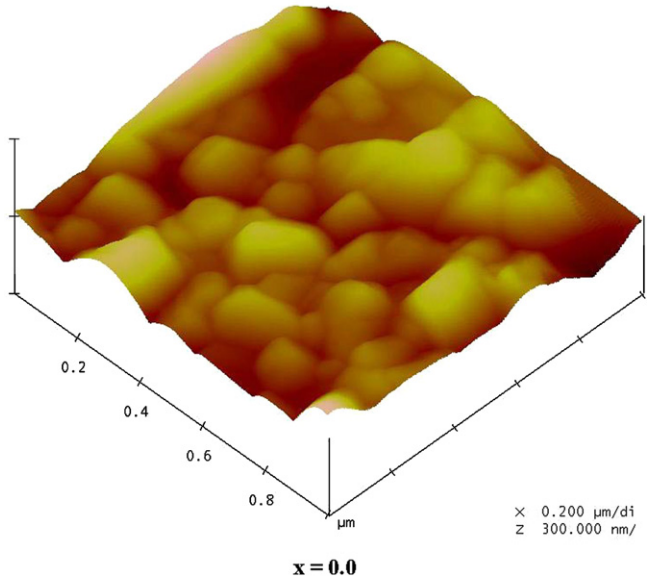

Fig. 5. AFM image of the typical sample (x=0.0) of $Ni_{0.5}Mg_{0.5}Fe_{2-x}Cr_xO_4$.

Cr^{3+} content. Fig. 7 shows the SEM images of the sintered pellet samples of the typical compositions of $Ni_{0.5}Mg_{0.5}Fe_{2-x}Cr_xO_4$. It is observed from Figs. 6 and 7 that the SEM images of the sintered pellets sample (Fig. 7) show dense structure as compared to that of powder sample (Fig. 6). We have calculated the bulk density of the sintered pellet samples using the Archimedes principle. It is observed that the bulk density decreases from 4.83 (x=0.0) to 4.62 (x=1.0) g/cm^3 with increasing Cr substitution. The decrease in bulk density for Cr substituted ferrite is mainly related to the decrease in crystallite size.

The shape, size and morphology of the particles were also examined by direct observation via TEM. The typical TEM micrographs for x=0.4, 0.6 and 1.0 samples are given in Fig. 8. The observations reveal that the particles are approximately spherical in shape and slightly agglomerated. Fig. 8 also shows the selected area electron diffraction (SAED) pattern for x=0.4, 0.6 and 1.0 samples. Diffraction rings can be clearly seen in Fig. 8, this indicates the polycrystalline nature of the prepared sample. Histograms (Fig. 9) show the size distribution of the presently investigated nanoparticles.

3.1.1. FT-IR spectroscopy

The FT-IR spectra of the chromium-substituted nickel–magnesium ferrite were recorded at room temperature in the frequency range of 400–4000 cm^{-1} and the obtained results are shown in Fig. 10. The higher frequency band (v_1=585–681 cm^{-1}) and lower frequency band (v_2=440–452 cm^{-1}) are assigned to the tetrahedral and octahedral sites respectively [15]. The normal mode of vibration of the tetrahedral cluster is higher than that of the octahedral cluster. It could be attributed to the shorter bond length of the tetrahedral cluster and longer bond length of the octahedral cluster. The FT-IR spectra also show the absorption bands in the region of 1100–1300 cm^{-1} corresponding to NO_3 ions; an absorption band corresponding to carboxyl group (COO^-) is observed at around 1700 cm^{-1} and one more at 3000–3700 cm^{-1} corresponding to the hydrogen bonded O–H groups. Owing to the high temperature generated during the combustion process all the carboxyl, hydroxyl and nitrate groups appear with less intensity.

3.1.2. UV–visible spectroscopic studies

The UV–visible spectra of the typical samples (Fig. 11) shows the absorption band at around 290 nm, which originates primarily from the absorption and scattering of UV radiation by the magnetic nanoparticles. UV/visible spectra show that the electronic structures of these ferrites slightly change with the increasing x. In the present ferrite

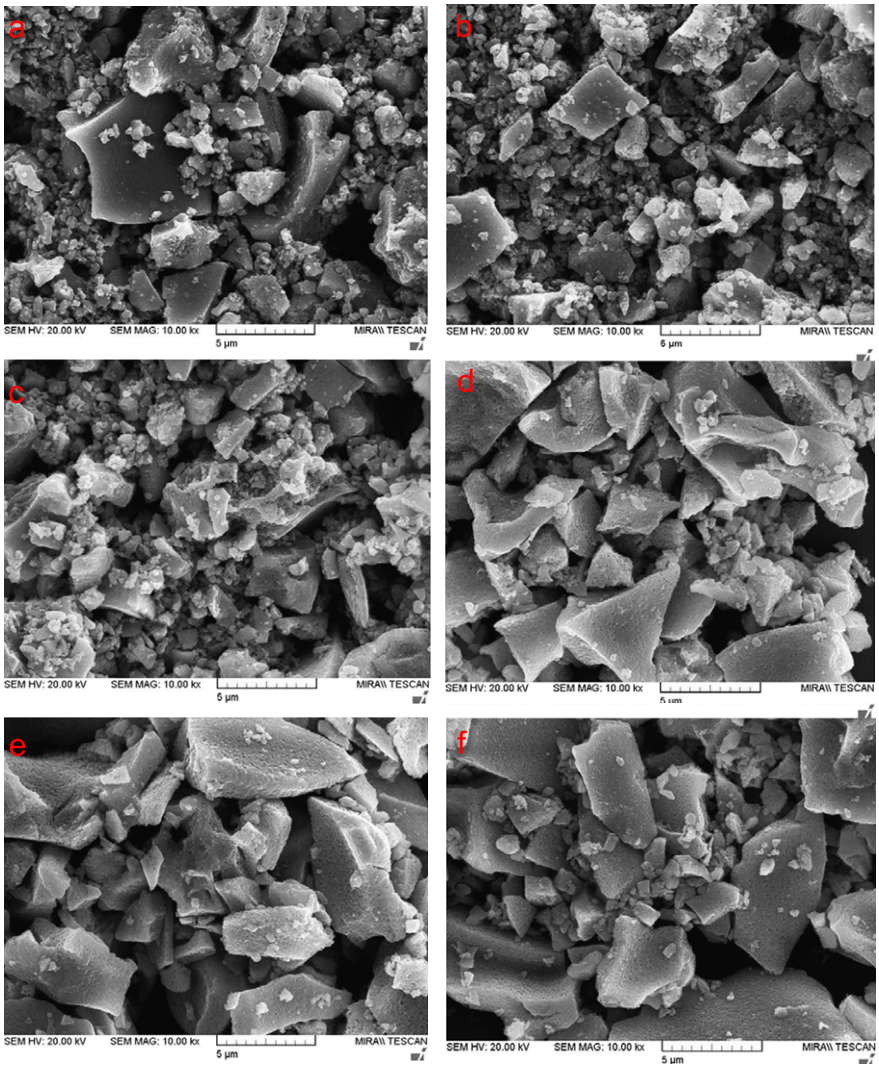

Fig. 6. SEM images of the powder samples (a) $x=0.0$, (b) $x=0.2$, (c) $x=0.4$, (d) $x=0.6$, (e) $x=0.8$ and (f) $x=1.0$.

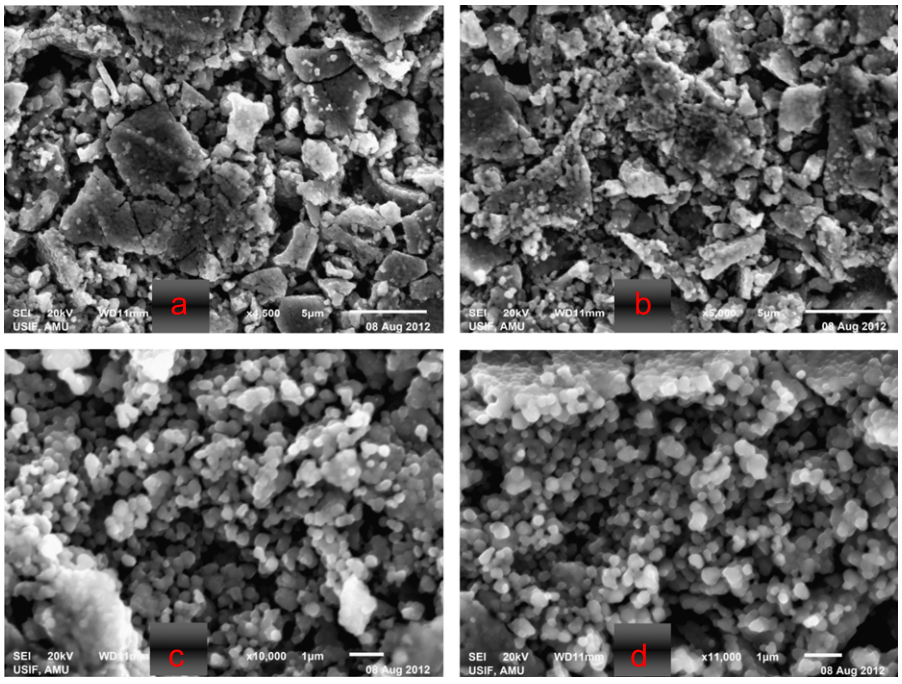

Fig. 7. SEM images of the sintered pellets of the typical samples (a) $x=0.2$, (b) $x=0.4$, (c) $x=0.6$ and (d) $x=0.8$.

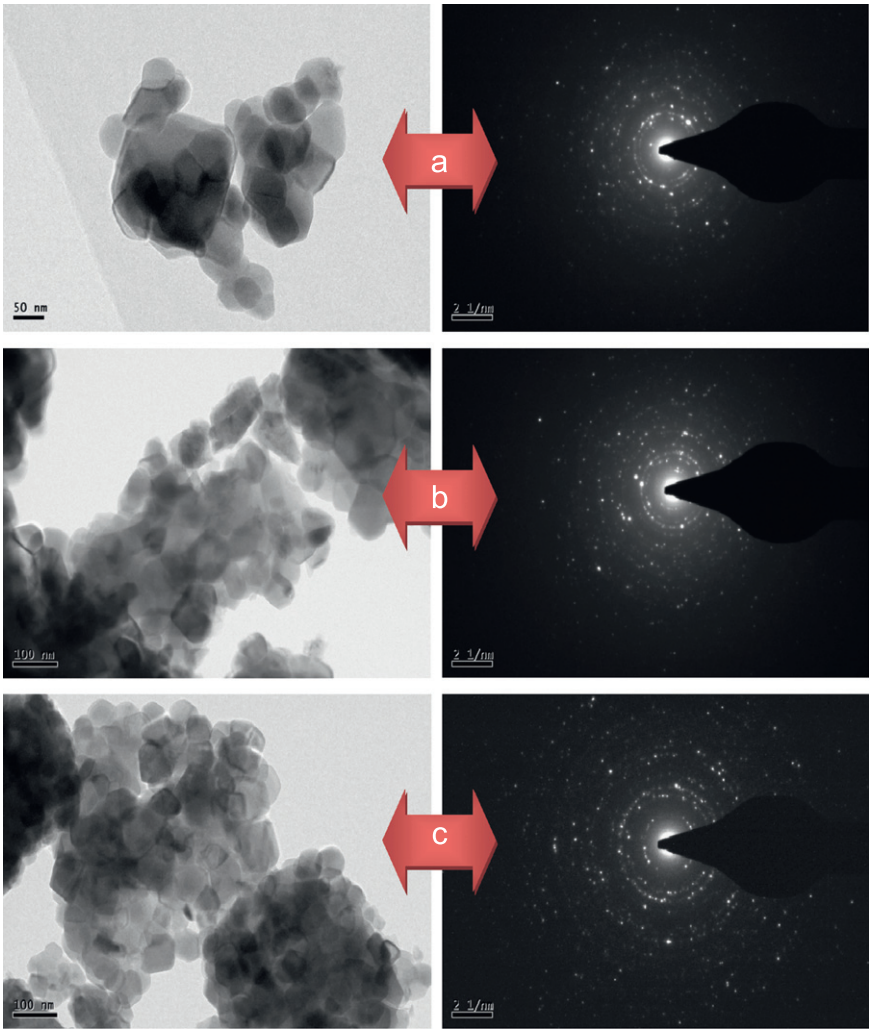

Fig. 8. TEM and their respective SAED images of the typical samples (a) $x=0.4$, (b) $x=0.6$ and (c) $x=1.0$.

system, when Fe^{3+} ions are replaced by Cr^{3+}, the absorbances of ferrites at same wavelengths diminish with increasing Cr^{3+} substitution, which may be due to fewer Fe^{3+} ions in the samples. However, the overall shape of the absorbance spectra is similar for all the samples. In general, the absorbances at lower wavelengths decrease considerably and do not depend on x, which may be due to the change in the particle size, particle shape, and dispersibility of these ferrites on calcinations.

3.1.3. Dielectric behavior

The dielectric properties of ferrites strongly depend on several factors, including the method of preparation, chemical composition, and grain size. Figs. 12 and 13 depict the variation of the real (ε') and imaginary (ε'') part of the dielectric constant as a function of an ac field at room temperature in the frequency range of 42 Hz–5 MHz. It is clearly evident from these figures that the dielectric constant initially decreases rapidly in the low frequency region but at very high frequencies its value becomes so small that it becomes independent of applied frequency. The low-frequency dispersion in ferrites is observed due to a space-charge effect [16]. The imaginary part of dielectric constant (ε'') decreases with increasing frequency at a faster rate than the real part of dielectric constant (ε'). The observed behavior can be explained on the basis of interfacial polarization suggested by Koops [17]. During the sintering process the presence of majority Fe^{3+} ions and minority Fe^{2+} ions makes the ferrite material dipolar, as Fe^{2+} ions are usually formed due to the partial reduction of Fe^{3+} ions during the synthesis process. The electron exchange interaction between the ferrous (Fe^{2+}) and ferric (Fe^{3+}) ions results in the local displacement of the electrons in the direction of the applied field which determines the polarization in ferrites. The decrease in dielectric constant with increasing frequency is explained to be due to the decrease of polarization of the dipoles when electric field propagates with high frequency. In other words beyond a certain frequency region or electric field the electron exchange does not follow the applied alternating field. The high value of the dielectric constant at lower frequency region is due to the existence of Fe^{2+} ions, oxygen vacancies, grain boundary defects, etc [18,19]. While the decrease in dielectric constant with frequency is

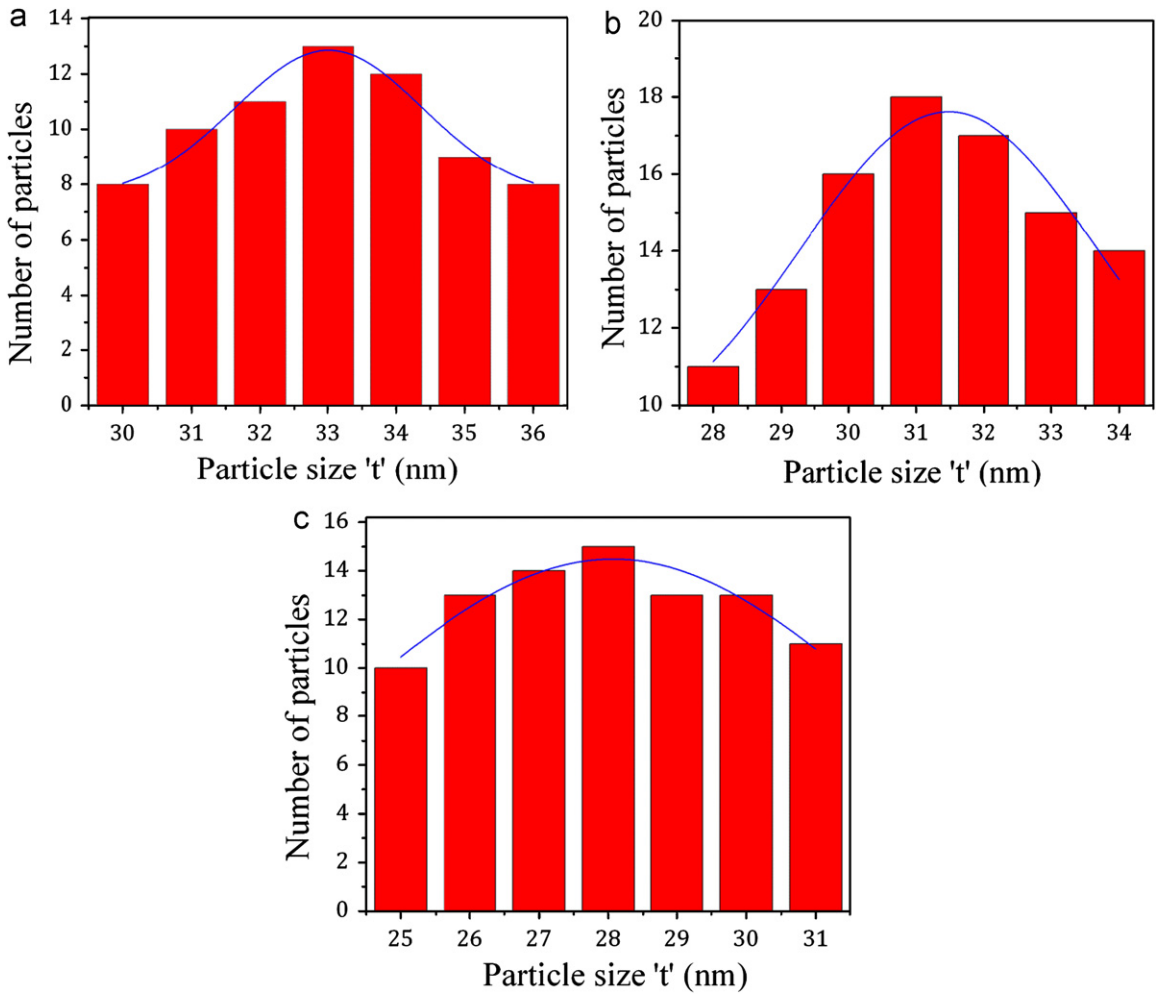

Fig. 9. Size distribution of nanoparticles from TEM images (a) $x=0.4$, (b) $x=0.6$ and (c) $x=1.0$.

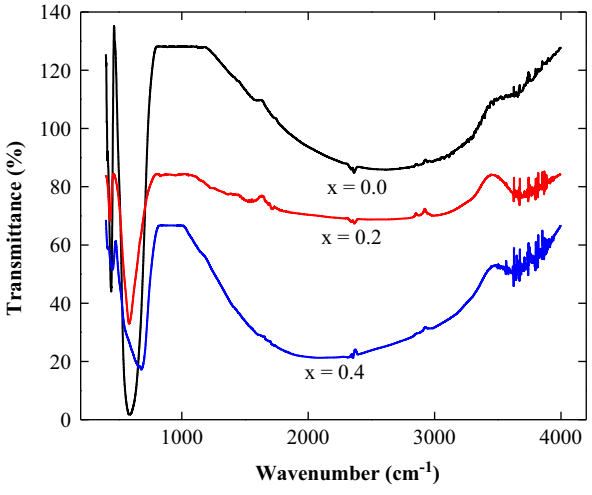

Fig. 10. FT-IR spectra of $Ni_{0.5}Mg_{0.5}Fe_{2-x}Cr_xO_4$ (for $x=0.0$, 0.2 and 0.4) ferrite nanoparticles.

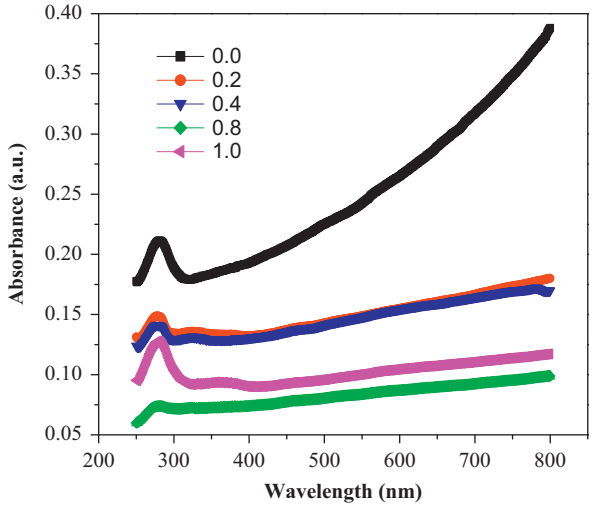

Fig. 11. The UV/visible absorption spectra of $Ni_{0.5}Mg_{0.5}Fe_{2-x}Cr_xO_4$ samples with different x values.

natural, i.e., any species contributing to the polarizability is found to show lagging behind the applied field at higher frequencies [20]. A plot of dielectric loss tangent (tan δ) versus frequency at room temperature is shown in Fig. 14. The value of tan δ measures the loss of electrical energy from the applied electric field into the samples at different

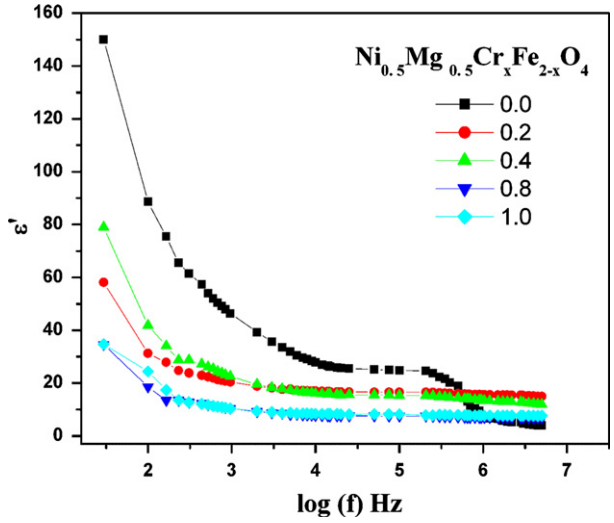

Fig. 12. Variation of real part i.e. dielectric constant (ε') as a function of $\log f$.

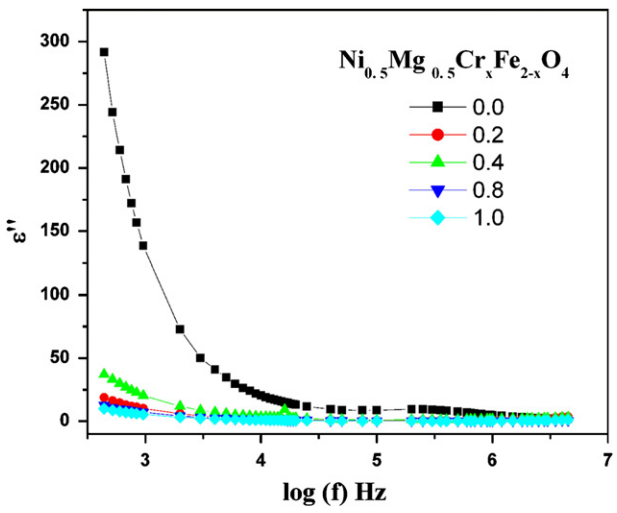

Fig. 13. Variation of imaginary part i.e. dielectric constant (ε'') as a function of $\log f$.

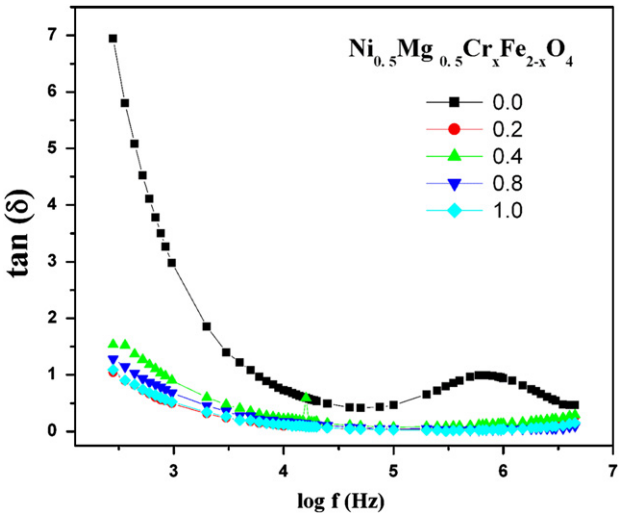

Fig. 14. Variation of dielectric loss tangent (tan δ) as a function of $\log f$.

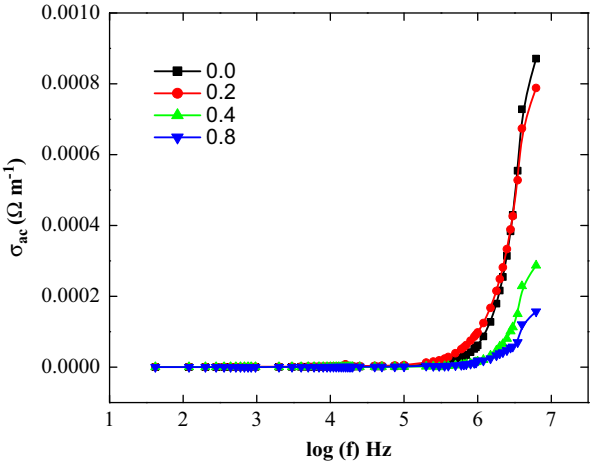

Fig. 15. Variation of σ_{ac} conductivity with $\log f$.

frequencies. It is observed that the tan δ shows a decreasing trend with increase in frequency. All the samples shows normal behavior except $x=0.0$. In the case of pure Ni–Mg ferrite ($x=0.0$) normal behavior is obtained up to 2 MHz and after that the peaking behavior is observed. This type of peaking behavior (Debye-type relaxation) is observed when the jumping frequency of the $Fe^{2+}$and Fe^{3+} ions is exactly equal to the frequency of applied field [21]. The dielectric loss is more at high frequency because of increase in interruption to the passage of electric field through the sample due to its interaction with the oscillating majority charges carriers of the dipoles.

Further, it is observed from Figs. 12–14 that the dielectric constant, dielectric loss and dielectric loss tangent decreased with Cr^{3+} substitution. This behavior can be explained by using the assumption that the mechanism of dielectric polarization is similar to that of conduction in ferrites. According to this, the electronic exchange interaction between $Fe^{2+} \leftrightarrow Fe^{3+}$ results in a local displacement of the electrons in the direction of an electric field which determines the polarization of ferrites. The presence of Fe^{2+} ions in excess amount favours the polarization effects [22]. Thus, more dispersion observed in the sample with low Cr^{3+} ion substitution can be attributed to the presence of Fe^{2+} ions in excess amount. As the Cr^{3+} ions substitution increased which replaces Fe^{3+} ions, and the Fe^{3+} ions are reduced in the samples, there is less possibility of electronic exchange interaction between $Fe^{2+} \leftrightarrow Fe^{3+}$, which results in decrease in dielectric parameters.

3.1.4. Frequency dependence of ac-conductivity

Conductivity is the physical property of a material which characterizes the conducting power inside the material.

The electrical conductivity in ferrite is mainly due to the hopping of electrons between the ions of the same element present in more than one valence state and distributed randomly over crystallographically equivalent sites. The total frequency dependence of ac conductivity is expressed as

$$\sigma\text{tot}' = \sigma o(T) + \sigma(\omega, T) \quad (3)$$

where the first term is dc conductivity which is due to the band conduction and is frequency independent. The second term is pure ac conductivity due to the hopping processes at the octahedral site and it is a frequency dependent function. The first term is predominant at low frequencies and at high temperature, while the second term is predominant at high frequencies and at low temperature. The frequency dependence of the second term σ_{ac} can be written as

$$\sigma_{ac} = A\omega^{n} \quad (4)$$

where A is a constant having the units of conductivity, and the exponent 'n' is a temperature dependent constant, σ is the real part of the conductivity, ω is angular frequency ($\omega = 2\pi f$), and 'n' is an exponent. To understand the effect of the conduction and types of polaron contributing for conduction, the variation of ac conductivity of nanophase chromium substituted nickel–magnesium ferrites was studied at different frequencies (42–5 Hz) and is illustrated in Fig. 15.

Fig. 16 shows the variation of $\ln \sigma$ versus $\ln \omega$ in the frequency range of 42 Hz–5 MHz, measured at room temperature. The ac conductivity shows an increasing trend with the increase in frequency for all the compositions. Its value first increases linearly according to the power law Eq. (4). It is seen that the conductivity of as prepared ferrite shows a gradual rise at low frequencies whereas at higher frequencies the conductivity rises steeply. This behavior can be explained on the basis that at low frequencies the conductivity is found low due to the grain boundary effect which acts as a hindrance for mobility of the charge carriers. At high frequency regions the conductivity is mainly due to the ionic part which makes the effect due to the grain boundaries. The linear increase in ac conductivity with the frequency confirms the polaron type of conduction [23]. Finally, low values of conductivity around room temperature indicate that the studied compositions may be good candidates for the microwave applications that require negligible eddy currents [24]. The values of exponent n were derived from the slope of the curves in Fig. 15. Fig. 17 shows the variation of n as a function of Cr concentration. It can be seen that the exponent n is found to be composition dependent. It is reported that n has values between 0 and 1. In the present study the values of the exponent n varies in the range 0.91–0.94.

3.1.5. Impedance

The concept of impedance was first introduced by Oliver Heaviside. Impedance spectroscopy is a specific branch of the tree of electrical measurements [25]. It has been among the most useful investigating techniques since the impedance of the grains can be separated from the other sources of impedance, namely grain boundaries and electrode effects [26]. Fig. 18 shows the complex impedance or Cole–Cole plot as a function of frequency at room temperature. There is no complete semicircle obtained except $x=0.0$. All the samples show one semicircle that is due to the conduction of the grain boundary, suggesting that a predominant conduction is through the grain boundary volume. Furthermore, contribution from the grain is not well resolved in all the samples. It is therefore concluded that the conductivity for all the samples is mainly due to the grain boundary contribution.

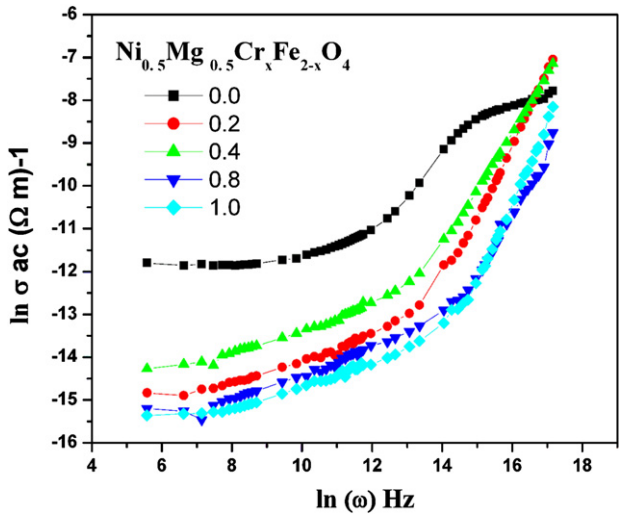

Fig. 16. Variation of ln ac conductivity with log ω.

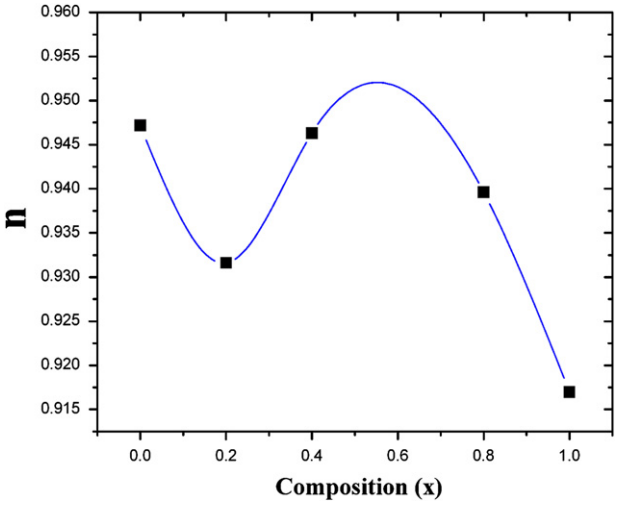

Fig. 17. Indexed exponent value 'n' with Cr concentration of $Ni_{0.5}Mg_{0.5}Fe_{2-x}Cr_xO_4$.

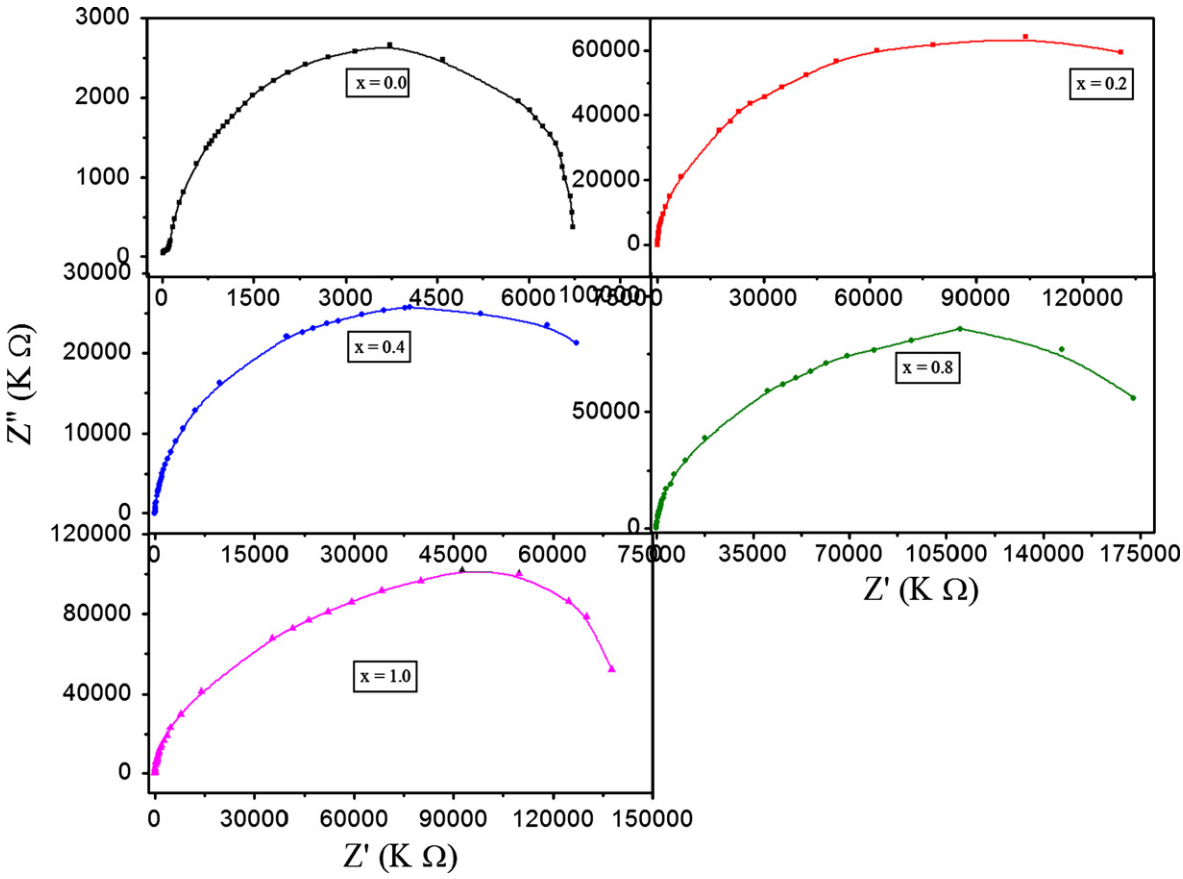

Fig. 18. Cole–Cole plots of $Ni_{0.5}Mg_{0.5}Fe_{2-x}Cr_xO_4$ ferrite nanoparticles at room temperature.

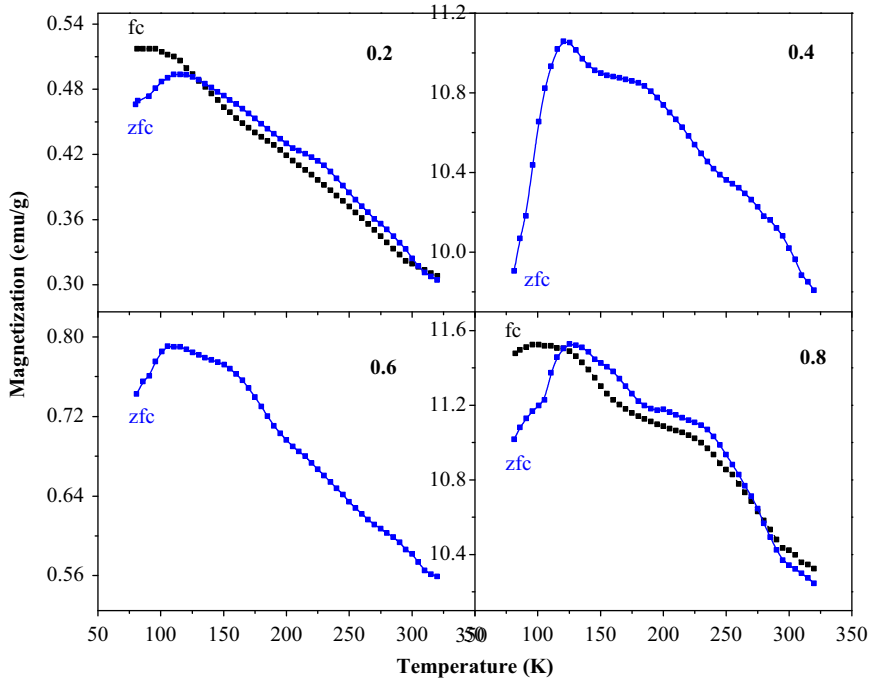

Fig. 19. Plots of temperature dependence of magnetic susceptibility for field cooled (FC) and zero-field cooled (ZFC) for x=0.2, 0.4, 0.6 and 0.8 at applied field of 100 Oe.

3.1.6. FC/ZFC

Fig. 19 shows the variation of magnetization with temperature curves in an external field of 100 Oe recorded in zero field cooled (ZFC) and field cooled (FC) modes. Fig. 19 also shows a divergence between the ZFC and FC curve, which is a characteristic feature of super paramagnetic behavior, and is attributed to the temporal relaxation. Such a divergence originates from the anisotropy barrier blocking of the magnetization orientation in the nano-particles cooled with a ZFC process [27]. A peak in the magnetization is evident in each case with the position of the peak varying with the Cr^{3+} substitution. It is understood that in the ZFC mode the magnetization is a collection of nanoparticles which may go through a peak as the particles' moments become blocked along the anisotropy axes. The blocking temperature (T_B) is defined as the temperature at which maximum magnetization is achieved. It is observed that the blocking temperature increased with the increase in Cr^{3+} substitution. The higher anisotropy of Cr^{3+} ions compared to that of Fe^{3+} leads to an overall increase of the anisotropy energy, resultantly decreasing the probability of a jump across the anisotropy barrier and hence the blocking temperature is shifted to a higher value.

4. Conclusions

The substitution of chromium ion in the $Ni_{0.5}Mg_{0.5}Fe_{2-x}Cr_xO_4$ ferrites causes significant changes in the structural, electrical and magnetic properties. Structural analysis with the XRD measurements reveals that the system confirms the formation of Ni–Mg ferrite. The lattice constant decreases proportionally to the chromium content. The dielectric constant and loss factors decrease with increasing frequency for all the samples. The dielectric parameters also decreased with increase in Cr^{3+} substitution. FT-IR spectral studies show the presence of two vibrational bands corresponding to the tetrahedral and octahedral sites. The ac conductivity data shows that the conduction process is the hopping type. Impedance analysis shows that the conduction mechanism is due to the grain boundary. Magnetic analysis confirm that the samples show ferrimagnetic behavior. The super paramagnetic blocking temperature has been found to increase linearly with increasing Cr substitution that has been understood to be due to the larger magneto crystalline anisotropy of Cr-ions as compared to Fe-ions that increases the chances of a jump across the anisotropy energy barrier.

Acknowledgments

Financial assistance from U.G.C. is acknowledged by Mohd. Hashim through Grant no. MANF-MUS-UTT-1092. This work is also supported by the Center of Excellence in Materials Science (Nanomaterials), Department of Applied Physics, Aligarh Muslim University, Aligarh, India.

References

[1] Alex Goldman, in: Modern Ferrite Technology, second ed., Springer, New York, 2006.
[2] Sagar E. Shirsath, R.H. Kadam, Anil S. Gaikwad, Ali Ghasemi, Akimitsu Morisako, Effect of sintering temperature and the particle size on the structural and magnetic properties of nanocrystalline $Li_{0.5}Fe_{2.5}O_4$, Journal of Magnetism and Magnetic Materials 323 (2011) 3104–3108.
[3] J. Smith, H.P.J. Wijn, Ferrites, Wiley, New York, 1959.
[4] C. Kittle, Theory of the structure of ferromagnetic domains in films and small particles, Physical Review 70 (1946) 965–971.
[5] V. Sepelak, A.D. Baabe, D. Mienert, F.J. Litterst, K.D. Becker, Enhanced magnetisation in nanocrystalline high-energy milled $MgFe_2O_4$, Scripta Materialia 48 (2003) 961–966.
[6] C.N. Chinnasamy, A. Narayanasamy, N. Ponpandian, K. Chattopadhyay, K. Shinoda, J. Jeyadevan, T. Tohji, K. Nakatsuka, T. Furubayashi, I. Nakatani, Mixed spinel structure in nanocrystalline $NiFe_2O_4$, Physical Review B (2001) 184108.
[7] V. Pillai, D.O. Shah, Synthesis of high-coercivity cobalt ferrite particles using water-in-oil microemulsions, Journal of Magnetism and Magnetic Materials 163 (1996) 243–248.
[8] Y. Ahn, E.J. Choi, S. Kim, H.N. Ok, Magnetization and Mössbauer study of cobalt ferrite particles from nanophase cobalt iron carbonate, Materials Letters 50 (1) (2001) 47–52.
[9] S.T. Alone, Sagar E. Shirsath, R.H. Kadam, K.M. Jadhav, Chemical synthesis, structural and magnetic properties of nanostructured Co–Zn–Fe–Cr ferrite, Journal of Alloys and Compounds 509 (2011) 5055–5060.
[10] B.G. Toksha, Sagar E. Shirsath, M.L. Mane, S.M. Patange, S.S. Jadhav, K.M. Jadhav, Auto-combustion high-temperature synthesis, structural and magnetic properties of $CoCr_xFe_{2-x}O_4$ ($0 \le x \le 1.0$), Journal of Physical Chemistry C 115 (2011) 20905–20912.
[11] M.A. Gabal, Y.M. AlAngari, Low-temperature synthesis of nanocrystalline NiCuZn ferrite and the effect of Cr substitution on its electrical properties, Journal of Magnetism and Magnetic Materials 322 (2010) 3159–3165.
[12] Mohd. Hashim, Alimuddin, Shalendra Kumar, Sikander Ali, B.H. Koo, H. Chung, Ravi Kumar, Structural, magnetic and electrical properties of Al^{3+} substituted Ni–Zn ferrite nanoparticles, Journal of Alloys and Compounds 511 (2012) 107–114.
[13] A.R. Denton, N.W. Ashcroft, Vegard's law, Physical Review A 43 (1991) 3161–3164.
[14] B.D. Cullity, in: Elements of X-ray Diffraction, Addison–Wesley Publ. Comp. Inc., Reading, Massachusetts, USA, 1956, p. 99.
[15] R.D. Waldron, Infrared spectra of ferrites, Physical Review 99 (1955) 1727–1735.
[16] R. Laishram, S. Phanjoubam, H.N.K. Sarma, C. Prakash, Electrical and magnetic studies of the spinel system $Li_{0.5+t}Cr_xSb_tFe_{2.5-x-2t}O_4$, Journal of Physics D: Applied Physics 32 (1999) 2151–2154.
[17] C.G. Koops, On the dispersion of resistivity and dielectric constant of some semiconductors at audio frequencies, Physical Review 83 (1951) 121–124.
[18] I.T. Rabinkin, Z.I. Novikova, Ferrites, Izv Acad. Nauk USSR Minsk, 1960.
[19] J.C. Maxwell, Electricity and Magnetism, vol. 2, Oxford University Press, New York, 1973.
[20] R.G. Kharabe, R.S. Devan, C.M. Kanamadi, B.K. Chougule, Dielectric properties of mixed Li–Ni–Cd ferrites, Smart Materials and Structures 15 (2006) 36–39.
[21] N. Rezlescu, E. Rezlescu, Dielectric properties of copper containing ferrites, Physica Status Solidi (a) 23 (1974) 575–582.
[22] Sagar E. Shirsath, B.G. Toksha, Maheshkumar L. Mane, V.N. Dhage, D.R. Shengule, K.M. Jadhav, Frequency, temperature and In^{3+} dependent electrical conduction in $NiFe_2O_4$ powder, Powder Technology 212 (2011) 218–223.
[23] M. Penchal Reddy, W. Madhuri, G. Balakrishnaiah, N. Ramamanohar Reddy, K.V. Siva Kumar, V.R.K. Murthy,

R. Ramakrishna Reddy, Microwave sintering of iron deficient Ni–Cu–Zn ferrites for multilayer chip inductors, Current Applied Physics 11 (2011) 191–198.

[24] M.A. Elkestawy, AC conductivity and dielectric properties of, $Zn_{1-x}Cu_xCr_{0.8}Fe_{1.2}O_4$ spinel ferrites, Journal of Alloys and Compounds 492 (2010) 616–620.

[25] Evgenij Barsoukov, J. Ross, Macdonald, Impedance Spectroscopy, Theory, Experiment, and Applications, second ed., John Wiley & Sons, 2005.

[26] J.T.S. Irvine, D.C. Sinclair, A.R. West, Electroceramics: characterization by impedance spectroscopy, Advanced Materials 2-3 (1990) 132–138.

[27] A.J. Rondinone, A.C.S. Samia, Z.J. Zhang, Superparamagnetic relaxation and magnetic anisotropy energy distribution in $CoFe_2O_4$ spinel ferrite nanocrystallites, Journal of Physical Chemistry B 103 (1999) 6876–6880.